Results in Physics 70 (2025) 108155

Contents lists available at ScienceDirect

Results in Physics

journal homepage: www.elsevier.com/locate/rinp

Pore-scale evaluation on hydrothermal performance in a microtube with homogeneous microporous media by lattice Boltzmann method

Saboura Yousefi [a], Mostafa Mahdavi [a,*], Seyed Soheil Mousavi Ajarostaghi [b], Mohsen Sharifpur [a,c,d,*], Magda Abd El-Rahman [e]

[a] Department of Mechanical and Aeronautical Engineering, University of Pretoria, Pretoria 0002, South Africa
[b] Mechanical Engineering Department, Université de Sherbrooke (UdeS), Sherbrooke, QC J1K 2R1, Canada
[c] School of Mechanical, Industrial and Aeronautical Engineering at the University of the Witwatersrand (Wits), South Africa
[d] Department of Medical Research, China Medical University Hospital, China Medical University, Taichung, Taiwan
[e] Department of Physics, College of Science, King Khalid University, Abha 61413, Saudi Arabia

ARTICLE INFO

Keywords:
Microtube
Lattice Boltzmann Method (LBM)
Microporous
Pore-Scale Modeling
Nanofluid
Hydrothermal

ABSTRACT

This study investigates the heat transfer and flow behavior of Al_2O_3-water nanofluid in micro-scale systems, using the lattice Boltzmann method (LBM) for numerical simulations. To implement the LBM code, FORTRAN home-made programming is employed. The research focuses on a three-dimensional microtube (500 μm diameter and 6,000 μm length) subjected to a uniform wall heat flux, with Reynolds numbers between 40 and 100. Spherical particles of varying sizes and quantities are introduced into the flow path to investigate the impact of porosity on thermophysical properties. The study explores the relatively unexamined application of the LBM to curved boundaries. Results indicate that introducing 6–10 spherical objects at Re = 40 increases the average Nusselt number by about 23.61 % and 25.83 %, respectively, whereas larger spheres in smaller quantities exhibit minimal or negative effects on heat transfer. Although the lattice Boltzmann method is gaining traction in fluid dynamics, its application to curved boundaries remains limited. This study advances the field by analyzing flow dynamics in a microtube with spherical inserts, integrating curved boundaries, nanofluids, and porous structures, thereby providing valuable insights into thermophysical studies.

Introduction

Nanofluids have garnered attention for their superior heat transfer capabilities compared to traditional fluids, especially in the thermal management of micro-electro-mechanical systems (MEMS) [1]. Choi [2] introduced the concept involving dispersing nanoparticles in base fluids to enhance their thermophysical properties. While numerous studies have explored the applications and properties of nanofluids [3–9], their practical implementation often overlooks critical factors such as flow dynamics in complex geometries or interactions with porous structures. Nanofluid performance factors include nanoparticle size and concentration, temperature, base fluid properties, and pH levels [10]. However, most research focuses on optimizing these factors under simplified conditions, leaving the impact of geometrical features like curved boundaries or internal inserts underexplored. Despite the promise of nanofluids in optimizing thermal systems [11], there is a lack of comprehensive studies addressing their behavior in microtubes with innovative designs.

Deploying micro-sized devices brings notable benefits, enhancing systems' economic and environmental aspects. As electronic devices rapidly evolve, the need for highly efficient thermal management systems intensifies. Microtubes and microchannels, often enhanced with advanced geometries or nanofluid applications, are critical in optimizing heat transfer. Beyond electronic cooling, these devices are pivotal in various industrial and research domains, including drug delivery, medical and pharmaceutical technologies, bioengineering, and biotechnical analyses. Microtube applications span biomedical and engineering fields, enabling advancements in diagnostics, therapeutic methods, and organ-on-a-chip models. Innovations include devices for parallel fluid flow and enhanced cancer therapies through targeted mechanisms [12–14].

Studying fluid flow and heat transfer in microtubes has been a focal point for many researchers. Rahmati et al. [15] examined non-

* Corresponding authors at: Department of Mechanical and Aeronautical Engineering, University of Pretoria, Pretoria 0002, South Africa.
E-mail addresses: u11297362@up.ac.za, saboura.yousefi@gmail.com (S. Yousefi), m.mahdavee@gmail.com (M. Mahdavi), seyed.soheil.mousavi.ajarostaghi@usherbrooke.ca (S.S. Mousavi Ajarostaghi), mohsen.sharifpur@up.ac.za (M. Sharifpur), majedah@kku.edu.sa (M.A. El-Rahman).

https://doi.org/10.1016/j.rinp.2025.108155
Received 14 October 2024; Received in revised form 15 January 2025; Accepted 10 February 2025
Available online 12 February 2025

Nomenclature

c	Velocity vector
c_s	Speed of sound
c_p	Specific heat capacity [J.kg^{-1}.K^{-1}]
D_h	Hydraulic diameter [m]
d_p	Nanoparticle's diameter [m]
e_i	Lattice velocity direction
f	Distribution function
f_{eq}	Equilibrium Distribution Function
g	Temperature distribution function
g_{eq}	Equilibrium temperature distribution function
h	Convective heat transfer coefficient [W.m^{-2}.K^{-1}]
k	Thermal conductivity [W.m^{-1}.K^{-1}]
$\dot{m}$	Mass flow rate [kg.m^{-3}]
Nu	Nusselt number [-]
q	Heat flux [W.m^{-2}]
r_p	Nanoparticle's radius [m]
Re	Reynolds number [-]
t_l	Nanolayer thickness [m]
T	Temperature [K]
T_0	Absolut temperature [K]
T^*	Dimentinless temperature [-]
u	velocity [m.s^{-1}]
U^*	Dimentinless velocity [-]
w_i	Weight factor in ith direction
X	Dimensionless coordinate in X direction
Y	Dimensionless coordinate in Y direction
Z	Dimensionless coordinate in Z direction

Greek symbols

ν	Kinematic viscosity [m^2.s^{-1}]
φ	Volume concentration [-]
α	Heat diffusivity [m^2.s^{-1}]
τ	Relaxation time
ρ	Density [kg.m^{-3}]
μ	Dynamic viscosity [kg.m^{-1}.s^{-1}]

Subscripts

p	Particle
pe	Equivalent particle
f	Base fluid
w	Wall
b	Bulk
eff	Effective
nf	Nanofluid
l	Nanolayer
i	Discrete lattice directions

Abbreviations

LBM	Lattice Boltzmann Method
MD	Molecular Dynamics
MT	Microtube
CCF	Convergence Criteria Factor

Newtonian nanofluid flow in microtubes and highlighted how increased nanoparticle concentrations enhance heat transfer. However, their study focused on constant heat flux conditions and did not explore complex geometries or porous structures, which are key to further improving thermal performance. Salman et al. [16] investigated the laminar flow of nanofluids in microtubes and found that smaller particles and higher concentrations significantly enhance heat transfer. While insightful, their work was limited to straight microtubes and did not assess the impact of inserted objects or curved boundaries on flow dynamics and heat transfer. Salman et al. [17] explored forced convection in nanofluids experimentally and numerically, reporting a 22 % improvement for the SiO_2-water nanofluid. However, their analysis was restricted to basic geometries, neglecting the potential of design optimizations like porous or ribbed structures for enhancing heat transfer. Salman et al. [18] studied the effects of nanoparticle characteristics and heat flux on thermal performance, noting that the Nusselt number is independent of heat flux. However, the influence of complex boundary conditions, such as spherical inserts, was not addressed. Karimzadehkhouei et al. [19] demonstrated that higher inlet temperatures improve heat transfer in microchannels, particularly at the entrance. Nonetheless, their work primarily dealt with straight channels and did not examine the interplay of nanofluids with intricate geometrical features or porous media. While previous studies have significantly advanced the understanding of heat transfer in nanofluid-based systems, they often rely on simplified geometries and lack consideration of porous structures or curved boundaries. This study addresses these gaps by incorporating spherical inserts into microtubes, employing nanofluids, and using the Lattice Boltzmann Method to investigate flow and heat transfer dynamics under more complex and realistic conditions.

The Lattice Boltzmann Method (LBM) is a mesoscopic numerical approach derived from lattice gas automata (LGA). In this method, fluid behavior is modeled using discrete particles that move along predefined lattice directions, a process known as streaming, and interact at lattice nodes through collisions. LBM offers efficiency and versatility for simulating single-phase and multiphase flows. Its strength lies in managing complex geometries and multi-component systems. And the local nature of LBM's collision and streaming processes allows for high parallelizability, which can significantly reduce computational time on modern hardware. however, it's important to note that this claim may depend on the specific problem being solved, the grid resolution, and the implementation. In some cases, LBM's memory and computational requirements can increase due to its explicit nature and additional data storage for velocity distributions.[20–26]. Huang et al. [27] demonstrated the LBM's accuracy and efficiency over the Direct Simulation Monte Carlo (DSMC) method in analyzing slip gas flow in microtubes at Knudsen numbers between 0.01 and 0.1. Yang and Lia [28] showed the alignment of LBM and Control Volume Method results in analyzing Al_2O_3-water nanofluid flow at low Reynolds numbers, particularly for laminar flows. Xu et al. [29] applied the LBM to simulate spherical microparticle movement and sedimentation within a nanofluid flow microchannel, focusing on flow behavior and heat dissipation in nanofluid suspensions. Abdollahzadeh et al. [30] applied LBM to study the hydrothermal characteristics of Al_2O_3-water nanofluids at low Reynolds numbers, highlighting its applicability in thermal studies. Zhang and Liu [31] developed a 3D thermal lattice Boltzmann model to simulate magneto-hydrodynamic (MHD) convection in Czochralski silicon crystal growth. The model simplifies grid handling in cylindrical geometries using a coordinate transformation, enabling accurate melt flow and heat transfer simulations. Validated against experimental data, it shows that a transverse magnetic field stabilizes the system and extends the operational range of crystal growth parameters, offering valuable insights for optimizing CZ crystal production.

Mustafa et al. [26] investigated the mixed convection flow of copper/water nanofluids in a rectangular cavity using the Lattice Boltzmann Method (LBM). It examines the influence of magnetic fields and varying dimensions and positions of high-temperature obstructions (HOBs) on heat transfer. Results show that increasing the height of HOBs and positioning them closer to the cold wall significantly boosts the average Nusselt number, while higher Richardson numbers reduce heat transfer. The study provides valuable insights into optimizing heat transfer by

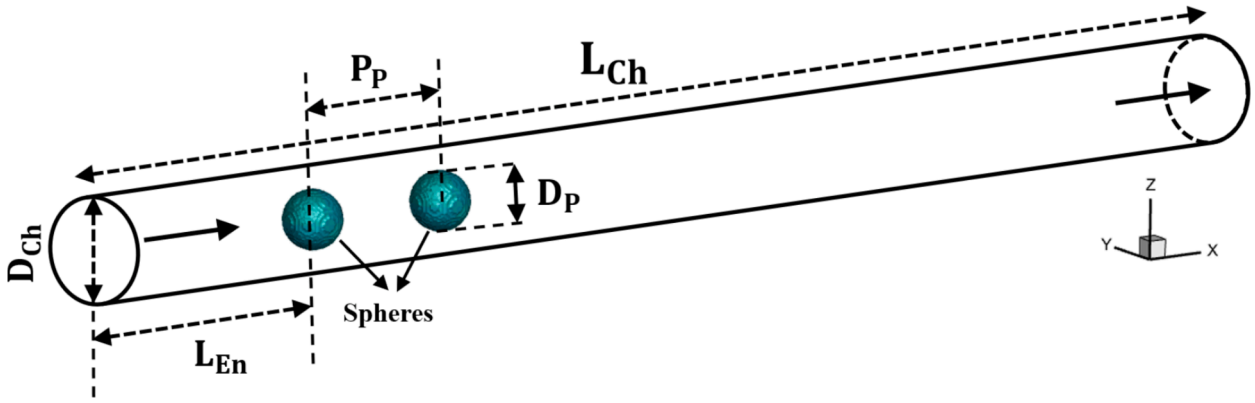

Fig. 1. Three-dimensional representation of the investigated microtube, including its geometric specifications.

manipulating obstruction geometry and magnetic field effects.

Recent advancements in Graphics Processing Unit (GPU) accelerated simulations have significantly enhanced computational efficiency and enabled more detailed investigations into complex fluid flow and heat transfer phenomena, as demonstrated in the following studies. Sorour Amini and Mohammadi [32] studied microparticle migration and separation in square microchannels using inertial microfluidics and dielectrophoresis (DEP). Particles settled near channel walls without an electric field, while an oscillating field shifted them by size and dielectric properties. GPU-accelerated simulations enabled a two-step method for efficient separation of polydisperse particles. Nee and Chamkha [33] developed a hybrid GPU-based CFD solver combining the lattice Boltzman and finite difference methods for 3D natural convection. The solver achieved over 30 × speedup but had stability issues at high Rayleigh numbers, limiting versatility. Akter et al. [34] examined non-Newtonian nanofluids in a porous cavity using GPU-accelerated MRT-LBM. Results showed more substantial buoyancy-enhanced heat transfer, with model validation confirming accuracy for porous media applications. Existing research often simplifies fluid behavior or neglects intricate interactions between nanoparticles and porous or dynamic geometries. This study addresses these limitations by leveraging LBM to analyze nanofluid behavior in advanced microtube configurations, emphasizing particle interactions and thermal enhancement mechanisms.

The thermophysical behavior of porous media significantly depends on the porous structures' size, geometry, and positioning, which influence flow and heat transfer characteristics. Numerous studies have explored these dynamics using various modeling techniques [35–41]. Wang et al. [42] investigated forced convection gas flow in porous microtubes, focusing on porosity, thermal conductivity ratio, Biot number, and porous material shape factor, all of which influence thermal and physical properties. Nojoomizadeh et al. [43] examined nanofluid flow in a partially porous microchannel, finding that reduced permeability and lower porosity enhance heat dissipation and thermal performance. Papazian et al. [44] compared solid and porous twisted tape inserts in cylindrical tubes, concluding that solid inserts provide better thermal performance due to their stronger mixing effects. Ibrahim et al. [45] Analyzed nanofluid flow in microtubes with twisted porous blocks, revealing that increasing the number of blocks raises the Nusselt number and improves heat transfer. Derikvand and Rahmati [46] demonstrated that porous disk inserts in microtubes with hydrophobic walls enhance the Nusselt number, with the thermal conductivity of the disks contributing more significantly than changes in size or positioning. Although these studies highlight the role of porous structures in enhancing heat transfer, many focus on simplified geometries or specific configurations. This research extends the understanding by examining complex porous geometries and their interactions with nanofluids in microscale systems, optimizing thermal performance through innovative designs.

Pore-scale modeling has been increasingly used to analyze heat transfer and flow in porous media, providing valuable insights into the impact of structural and dynamic factors. Zhu and Xuan [47] investigated concentrated solar power systems with porous media-based receivers, finding that higher porosity, smaller incident angles, and sphere surface absorptivity enhanced radiation propagation. They proposed a hybrid packed bed design to optimize thermal efficiency. Habib et al. [48] explored unsteady forced convection in porous media with cylindrical voids, highlighting the influence of Reynolds numbers on nonlinear flow behavior, particularly under fluctuating inlet flow conditions. Cheng and Wong [49] developed a method to assess heat transfer efficiency in packed beds filled with spherical particles, offering insights into heat transfer dynamics in reactors with finite-thickness walls under consistent external heating. Wang et al. [50] studied packed beds with internal heat sources, noting significant variations in fluid properties along the bed. They introduced a modified pressure drop model to address inaccuracies in conventional models, improving predictive accuracy. While these studies provide advancements in understanding pore-scale dynamics, they often rely on simplified configurations or focus on specific scenarios. This research builds on these findings by incorporating more complex geometries and varying heat sources to enhance the design and efficiency of porous media systems.

In recent years, significant efforts have been made to enhance heat transfer in microscale systems, particularly in microtubes used for thermal management in microelectronic devices and microelectromechanical systems. While the impact of porous materials on heat transfer has been extensively studied, limited research has examined their behavior within microtubes, especially in conjunction with nanofluids. This study addresses this gap by investigating the effects of spherical porous materials on heat transfer and fluid dynamics in microtubes. Specifically, this work explores their potential to improve thermal efficiency in microscale systems by analyzing their influence on nanofluid behavior under varying flow conditions. The findings have significant implications for enhancing the design of micro-cooling systems, improving the performance of heat exchangers in miniaturized devices, and optimizing the thermal management of high-performance microelectronics. In this work, home-made FORTRAN programming is used to implement the LBM code.

Numerical procedure

Problem description

This study investigates nanofluids' heat transfer and flow behavior within a microtube using the LBM in both single-phase and multi-phase configurations. The numerical model focuses on laminar forced convection and incompressible flow conditions. To analyze the effects of homogeneous microporous substances on nanofluid hydrothermal

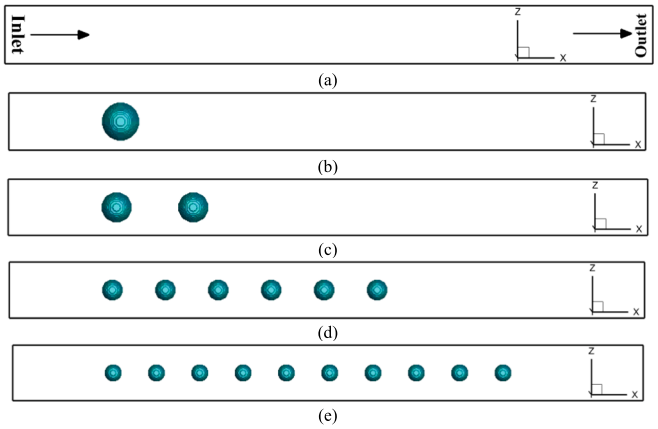

Fig. 2. Two-dimensional representation of the microtube configurations: (a) Standard microtube without spheres, (b) Configuration A featuring a single spherical object, (c) Configuration B with two spherical objects, (d) Configuration C containing six spherical objects, (e) Configuration D with ten spherical objects.

Table 1
Microtube dimensions for different arrangements.

Description	Symbol	Value [mm]
Microtube's Total Length	L_{Ch}	6
Microtube's Diameter	D_{Ch}	0.5
Entrance Length	L_{En}	0.9
Sphere's Diameter of Porous Arrangement 1 (One Sphere)	D_{P1}	0.36
Sphere's Diameter of Porous Arrangement 2 (Two Spheres)	D_{P2}	0.28
Spheres's Centre to Center Distance for Porous Arrangement 2	P_{P2}	0.72
Sphere's Diameter of Porous Arrangement 3 (Six Spheres)	D_{P3}	0.2
Spheres's Centre to Center Distance for Porous Arrangement 3	P_{P3}	0.5
Sphere's Diameter of Porous Arrangement 4 (Ten Spheres)	D_{P4}	0.166
Spheres's Centre to Center Distance for Porous Arrangement 4	P_{P4}	0.42

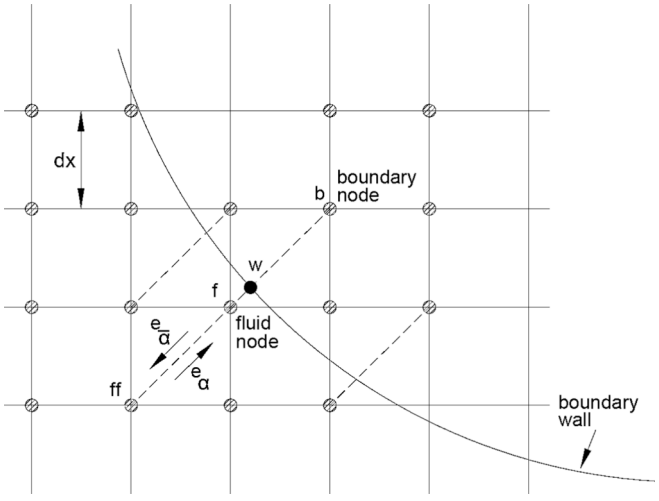

Fig. 3. Plan view of the boundary of the curved wall in two dimensions in LBM.

behavior, spherical objects were strategically inserted into the microtube as homogenous microporous media in various numbers and arrangements. Fig. 1 provides a 3D depiction of the microtube and spherical objects, detailing their geometrical parameters. Additionally,

Table 2
The thermal and physical properties of the material used [46].

Material	ρ [kg.m^{-3}]	k [W.m^{-1}.K^{-1}]	Cp [J.kg^{-1}.K^{-1}]	μ [kg.m^{-1}.s^{-1}]
Water	995.7	0.603	4183.0	7.98E-04
Al_2O_3	3600.0	39.2	765.0	–

Table 3
Comparison of microtube grid sizes.

Dimensions	T_{Outlet} [K]	Error [%]
40 × 40 × 456	314.71	–
50 × 50 × 570	321.92	2.240
60 × 60 × 684	323.075	0.358
70 × 70 × 798	323.089	0.004

Fig. 2 illustrates 2D schematics of different sphere configurations (A to E), maintaining a constant distance between centers equal to five times the sphere radius ($P_P = 2.5D_P$) across all arrangements. With a constant heat flux of 75 kW.m^{-2} on the microtube wall, the inlet conditions include an inlet temperature of 303 K and varying inlet velocities ranging from 0.032 to 0.16 m.s^{-1}. The study employs the Al_2O_3-water nanofluid with a 4 % volume concentration (ϕ = 4 %), assuming the working fluid is in thermal equilibrium and there is no slip at the boundary. Table. 1 summarizes the geometrical parameters outlined in Fig. 1.

Boundary and initial conditions

Physical boundary and initial conditions

The physical initial conditions applied to this study are as follows:

- The inlet temperature is maintained at 303 K.
- The inlet velocity of the nanofluid ranges from $V_{inlet} = 0.032$ m.s^{-1} to $V_{inlet} = 0.16$ m.s^{-1}, corresponding to Reynolds numbers between Re = 20 and Re = 100 (four values).
- Constant heat flux of 75 kW.m^{-2} is considered on the microtube wall.

Also, the physical boundary conditions applied to the microtube are detailed below:

- The inlet temperature at X = 0 is assigned as T_i = 303 K = 30 ℃.
- The inlet velocitis at X = 0 is assigned as u = u_i, v = 0, and r = 0.
- A no-slip boundary condition is imposed on the microtube's surface (u = 0, v = 0, and r = 0).

The boundary conditions applied to the spherical objects are detailed below:

- A no-slip boundary condition is imposed on the sphere's surface (u = 0, v = 0, and r = 0).
- At steady-state condition, the temperature of the fluid near the sphere surface is assumed to be in thermal equilibrium with the sphere surface temperature.

LBM boundary and initial conditions

The LBM initial conditions applied to this study are as follows:

- The inlet is maintained at T* = th (0, j, k) = 1.

The dimensionless inlet velocity in different directions is assumed as follows:

- u (0, j, k) = U*
- v (0, j, k) = 0.0
- r (0, j, k) = 0.0

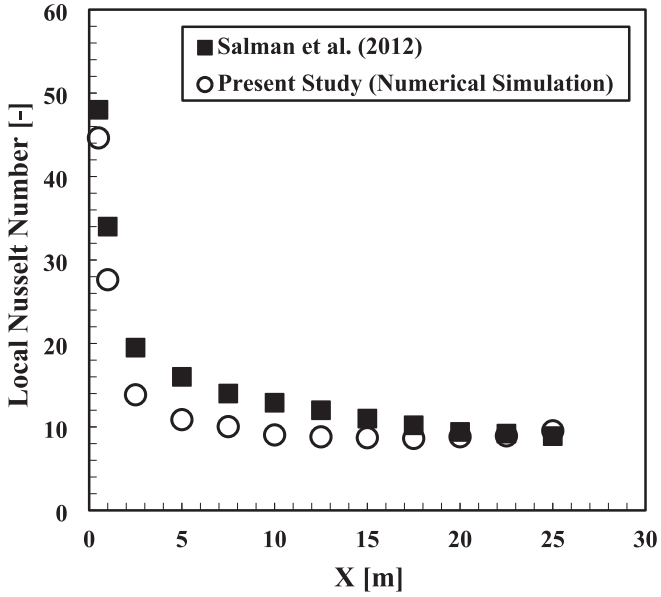

Distance	Experiment	Numerical Simulation	Error [%]
2.5	19.5	14.2	27.2%
7.5	14.0	10.0	28.3%
12.5	12.0	8.8	26.6%
17.5	10.2	8.6	15.5%
22.5	9.2	8.9	2.9%

(a)

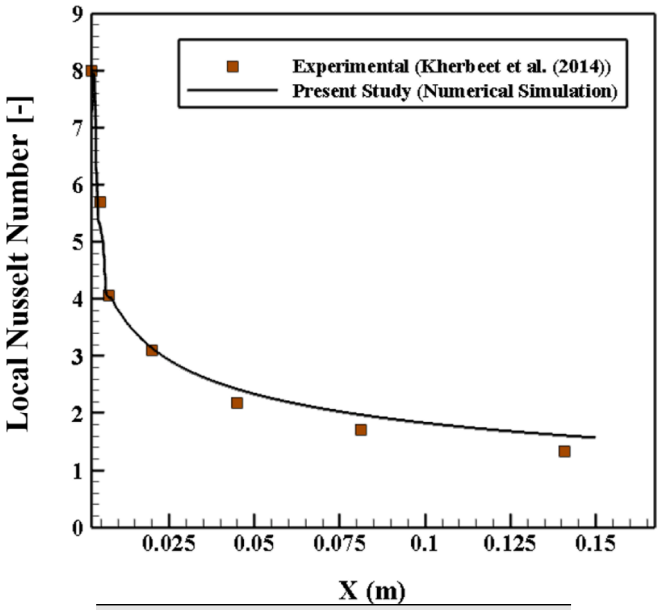

Distance	Experiment	Numerical Simulation	Error [%]
0.020	3.18	3.21	0.9%
0.045	2.21	2.41	8.3%
0.08	1.72	1.98	13.1%
0.14	1.35	1.61	16.1%

(b)

Fig. 4. (a) Evaluating the findings of the present LBM model concerning the results reported by Salman et al. [16] and (b) the comparison of the results of the present LBM work with the experimental results from Kherbeet et al. [59].

Table 4
The current LBM's average Nusselt numbers compared to Kays and Crawford's analytical findings [60].

Heat Flux Ratio (r_q)	Nu_1 (relative error %)		Nu_2 (relative error %)	
	Kays and Crawford [60]	LBM	Kays and Crawford [60]	LBM
0.5	17.48	17.25 (1.3 %)	6.51	6.49 (0.3 %)
1	8.23	8.16 (0.9 %)	8.23	8.16 (0.9 %)
1.5	11.19	11.10 (0.8 %)	7	6.91 (1.3 %)

where T* and U* are dimensionless temperature and velocity, respectively.

Also, the LBM boundary conditions applied to the microtube are detailed below:

- A no-slip boundary condition is imposed on the microtube's surface: (u (i, j, k) = 0, v (i, j, k) = 0, and r (i, j, k) = 0).
- The extrapolation method is utilized to determine the outlet temperature and velocity:$f_1(i,j,k) = 2 \times f_1(i-1.j.k) - f_1(i-2.j.k)$
- The thermal boundary condition applies to the microtube wall based on constant heat flux is $T(i.j+1.k) = T(i.j.k) + \frac{q.dx}{k}$.

Lattice Boltzmann method

The discrete approach in numerical simulations looks at molecules or atoms' movements and collisions and points out the position and

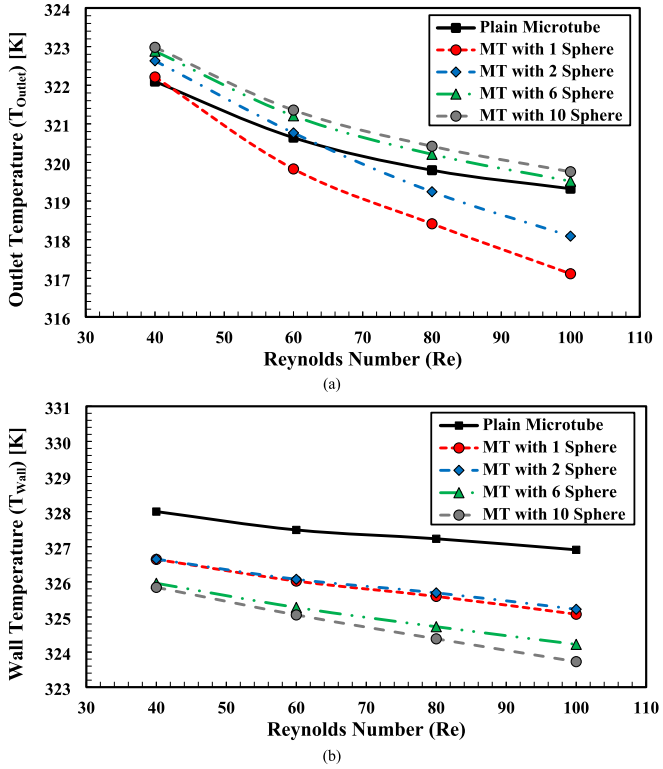

Fig. 5. Impact of sphere number on (a) the temperature at the microtube outlet and (b) the temperature of the microtube wall.

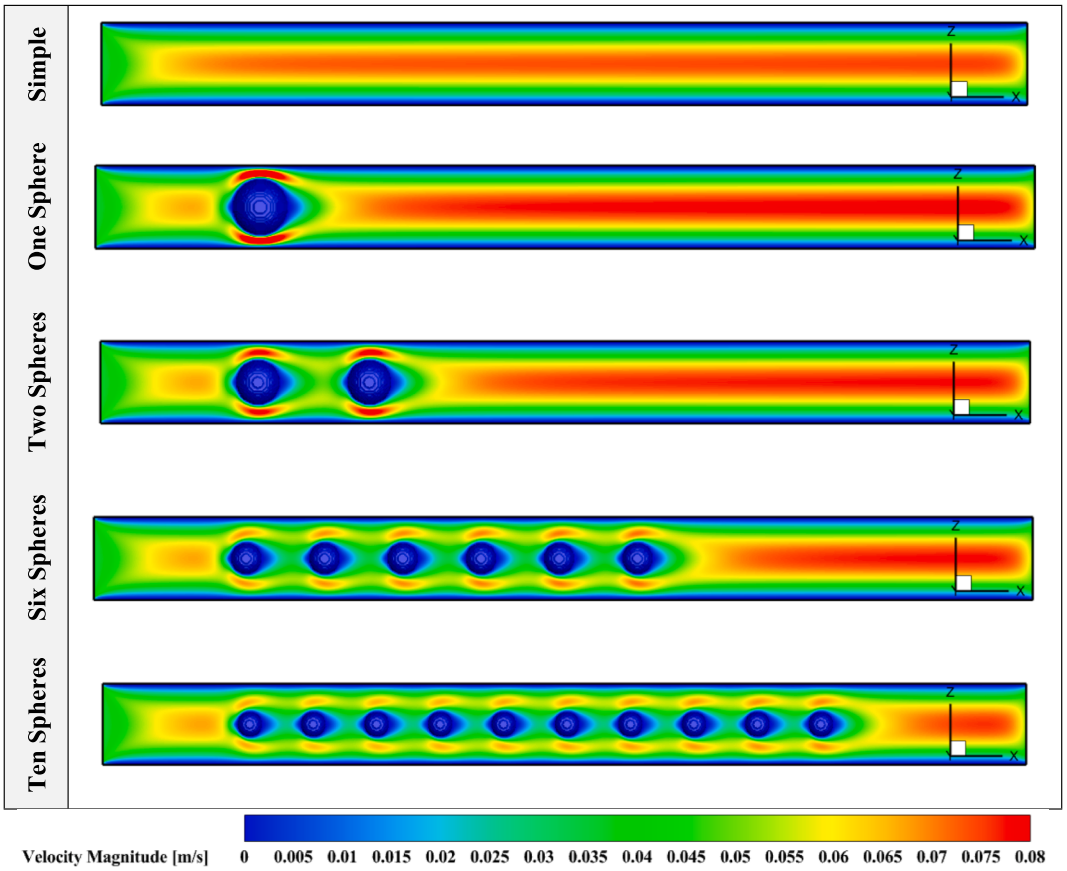

Fig. 6. Velocity magnitude contours in a computational domain slice (y/H = 30) for different scenarios.

velocity of each particle as tracked at every time step [51]. Molecular Dynamics (MD) considers a single particle's behavior, which is quite a convenient microscale study method for complex geometries and multiphase situations. However, the MD method's computation volume and duration are limitations in larger systems. LBM employs the mesoscopic scale and was initiated using the LGA method. Despite other discrete methods, LBM observes a cluster of particles instead of investigating individual particles. In LBM, the particle distribution function, $f(r,c,t)$, defines the count of particles within the interval r to $r + dr$, possessing velocities from c to $c + dc$ at time t. This simple discrete lattice equation, which is known as the working horse of the LBM, can be written as below [51]:

$$\frac{\partial f_i}{\partial t} + c_i \nabla f_i = \frac{1}{\tau}(f_i^{eq} - f_i) \tag{1}$$

$$\tau = 3\vartheta \frac{\Delta t}{\Delta x^2} + 0.5 \tag{2}$$

where f^{eq} denotes the equilibrium distribution function, τ stands for the relaxation factor, and i refers to multiple lattice orientations. The discretized representation of the equation in Cartesian coordinates is given by [51]:

$$f_i(\boldsymbol{r} + \boldsymbol{c_i}\Delta t, t + \Delta t) - f_i(\boldsymbol{r}, t) = \frac{\Delta t}{\tau}[f_i^{eq}(\boldsymbol{r}, t) - f_i(\boldsymbol{r}, t)] \tag{3}$$

$$f_i^{eq}(\boldsymbol{r}, t) = w_i \rho \left[1 + \frac{c_i.\boldsymbol{u}}{c_s^2} + \frac{(c_i.\boldsymbol{u})^2}{2c_s^4} - \frac{u^2}{2c_s^2}\right] \tag{4}$$

where

$$c_s = \frac{c}{\sqrt{3}} \tag{5}$$

$$c = \frac{\Delta x}{\Delta t} \tag{6}$$

About a study by Mei et al. [52], the D3Q19 method offers a good balance between computational reliability and efficiency for curved boundary studies, compared to other lattice Boltzmann configurations such as D3Q15 and D3Q27. Therefore, the D3Q19 model is applied in this study for velocity and temperature distribution functions.

Curved boundaries in LBM

Curved boundaries require more consideration in lattice Boltzman's analysis, and there is a lack of literature focusing on them. Some authors assumed curve boundaries as stairs for simplifying the solution, and according to Mei et al. [53], this simplification leads to the devaluation of accurate results.

Fig. 3 presents a plan view of the boundary of the curved wall in two dimensions. In this layout, bf is a link between two nodes, b in the solid and f in the fluid parts. The portion of this connection that resides within the fluid is denoted by Δ as follows [53]:

$$\Delta = \frac{|\boldsymbol{x}_f - \boldsymbol{x}_w|}{|\boldsymbol{x}_f - \boldsymbol{x}_b|} \tag{7}$$

The term e_α represents the discrete velocity moving from the fluid node toward the solid wall while $e_{\bar{\alpha}}$ denotes the discrete velocity in the opposite direction.

$$e_\alpha = -e_{\bar{\alpha}} \tag{8}$$

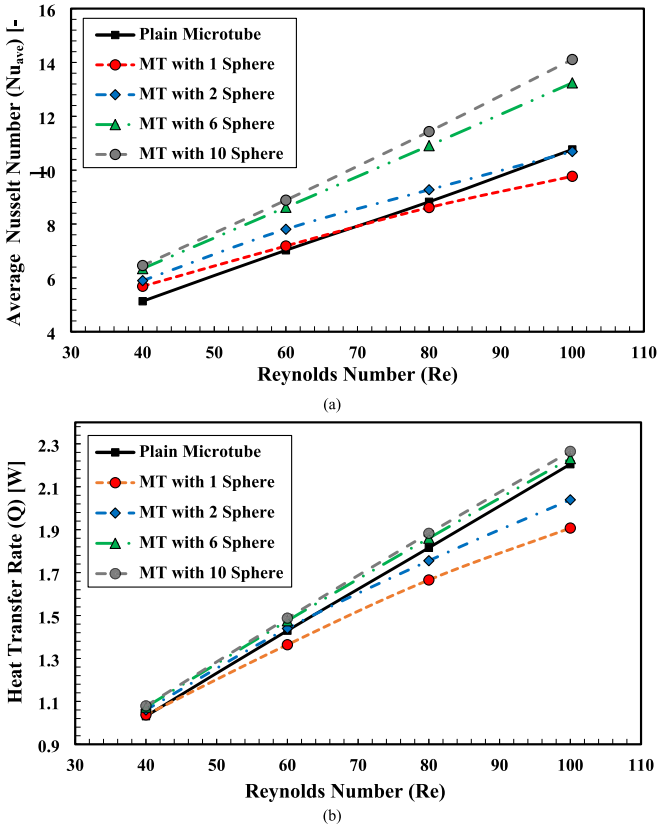

Fig. 7. (a) The impact of sphere number on the average Nusselt number, and (b) heat transfer rate variations versus the Reynolds number.

$$f_{\bar{\alpha}}(\boldsymbol{x}_f.t) \approx f_{\bar{\alpha}}^{(eq)}(\boldsymbol{x}_f.t) - \lambda e_{\bar{\alpha}} \bullet \nabla f_{\bar{\alpha}}^{(eq)}(\boldsymbol{x}_f.t) \tag{15}$$

$$f_{\bar{\alpha}}^{(eq)}(\boldsymbol{x}_f.t) = \rho w_\alpha \left[1 + \frac{3}{c^2}\boldsymbol{e}_{\bar{\alpha}} \bullet \boldsymbol{u} + \frac{9}{2c^4}(\boldsymbol{e}_{\bar{\alpha}} \bullet \boldsymbol{u})^2 - \frac{3}{2c^2}\boldsymbol{u} \bullet \boldsymbol{u}\right] \tag{16}$$

$$\nabla f_{\bar{\alpha}}^{(eq)}(\boldsymbol{x}_f, t) = \rho w_\alpha \frac{3}{c^2}\boldsymbol{e}_{\bar{\alpha}} \bullet \nabla \boldsymbol{u} \tag{17}$$

Applying the concept outlined below,

$$f_{\bar{\alpha}}^{(eq)}(\boldsymbol{x}_f, t) = f_\alpha^{(eq)}(\boldsymbol{x}_f, t) - 2\rho w_\alpha \frac{3}{c^2}\boldsymbol{u}_f \bullet \boldsymbol{e}_\alpha \tag{18}$$

And substituting Equations (16), (17), and (18) into Equation (15),

$$\begin{aligned} f_{\bar{\alpha}}(\boldsymbol{x}_f, t) &= f_\alpha^{(eq)}(\boldsymbol{x}_f, t) - 2\rho w_\alpha \frac{3}{c^2}\boldsymbol{u}_f \bullet \boldsymbol{e}_\alpha - \tau\delta t 2\rho w_\alpha \frac{3}{c^2}\boldsymbol{e}_\alpha \bullet \nabla \boldsymbol{u} \\ &\quad \bullet \boldsymbol{e}_\alpha \nabla f_{\bar{\alpha}}^{(eq)}(\boldsymbol{x}_f, t) \\ &= \rho w_\alpha \frac{3}{c^2}\boldsymbol{e}_{\bar{\alpha}} \bullet \nabla \boldsymbol{u} \end{aligned} \tag{19}$$

where,

$$\lambda = \tau\delta t \tag{20}$$

According to the equilibrium distribution function correlation [54]:

$$f_\alpha^{(eq)}(\boldsymbol{x}_f, t) = \rho w_\alpha \left[1 + \frac{3}{c^2}\boldsymbol{e}_\alpha \bullet \boldsymbol{u} + \frac{9}{2c^4}(\boldsymbol{e}_\alpha \bullet \boldsymbol{u})^2 - \frac{3}{2c^2}\boldsymbol{u} \bullet \boldsymbol{u}\right] \tag{21}$$

The correlation for $f_\alpha^{(*)}(\mathbf{x}_b, t)$ can be reformulated as follows [54]:

$$f_\alpha^{(*)}(\mathbf{x}_b, t) = f_\alpha^{(eq)}(\boldsymbol{x}_f, t) + \rho w_\alpha \frac{3}{c^2}\boldsymbol{e}_\alpha \bullet (u_{bf} - u_f) \tag{22}$$

From the equation above, the $\widetilde{f}_{\bar{\alpha}}(\boldsymbol{x}_b, t)$ can be formulated as [54]:

$$\begin{aligned} \widetilde{f}_{\bar{\alpha}}(\boldsymbol{x}_b, t) &\approx f_\alpha^{(eq)}(\boldsymbol{x}_f, t) + (1-\chi)(1-1/\tau) f_\alpha(\boldsymbol{x}_f, t) + w_\alpha \rho \frac{3}{c^2} e_\alpha . (\chi u_{bf} - \chi u_f - 2u_w) \\ &= f_\alpha^{(eq)}(\boldsymbol{x}_f, t) - (1-\chi)(\tau-1)\delta t w_\alpha \rho \frac{3}{c^2} e_\alpha . \nabla u . e_\alpha + w_\alpha \rho \frac{3}{c^2} e_\alpha . (\chi u_{bf} - \chi u_f - 2u_w) \end{aligned} \tag{23}$$

$$f_{\bar{\alpha}}(\boldsymbol{x}_f = \boldsymbol{x}_b + e_{\bar{\alpha}}\delta t.t + \delta t) = \widetilde{f}_{\bar{\alpha}}(\boldsymbol{x}_b.t) \tag{9}$$

To derive particle distribution function of node f in Fig. 2, the distribution function of node b is required. Filippova and Hanel [54] offered a linear interpolation technique:

$$\widetilde{f}_{\bar{\alpha}}(\boldsymbol{x}_b.t) = (1-\chi)\widetilde{f}_\alpha(\boldsymbol{x}_f.t) + \chi f_\alpha^{(*)}(\boldsymbol{x}_b.t) + 2\omega_\alpha \rho \frac{3}{c^2} e_{\bar{\alpha}} u_w \tag{10}$$

$$u_w \equiv u(x_w.t) \tag{11}$$

$$f_\alpha^{(*)}(x_b.t) = \omega_\alpha \rho(x_f.t)\left[1 + \frac{3}{c^2}e_\alpha \bullet u_{bf} + \frac{9}{2c^4}(e_\alpha \bullet u_f)^2 - \frac{3}{2c^2}u_f \bullet u_f\right] \tag{12}$$

$$u_f \equiv u(x_f.t) \tag{13}$$

u_f represents the velocity of the fluid in the node close to the boundary wall.

$$\boldsymbol{u}_{bf} = (\Delta - 1)\boldsymbol{u}_f/\Delta + \boldsymbol{u}_w/\Delta \tag{14}$$

Assuming Slow Flow condition and applying Chapman–Enskog expansion, the following correlations are applied by Filippova and Hanel [54]:

From Equations (19), (23), and (21):

$$\begin{aligned} &f_\alpha^{(eq)}(\boldsymbol{x}_f, t) - (1-\chi)(\tau-1)\delta t w_\alpha \rho \frac{3}{c^2} e_\alpha . \nabla u . e_\alpha + w_\alpha \rho \frac{3}{c^2} e_\alpha . (\chi u_{bf} - \chi u_f - 2u_w) \\ &= f_\alpha^{(eq)}(\boldsymbol{x}_f, t) - 2\rho w_\alpha \frac{3}{c^2}\boldsymbol{u}_f \bullet \boldsymbol{e}_\alpha - \tau\delta t 2\rho w_\alpha \frac{3}{c^2}\boldsymbol{e}_\alpha \bullet \nabla \boldsymbol{u} \bullet \boldsymbol{e}_\alpha \end{aligned} \tag{24}$$

$$\begin{cases} u_{bf} = \dfrac{(\Delta-1)u_f}{\Delta} + \dfrac{u_w}{\Delta} and \chi = (2\Delta - 1)/\tau for \Delta \geq \dfrac{1}{2} \\ u_{bf} = u_f and \chi = (2\Delta - 1)/(\tau - 1) for \Delta < \dfrac{1}{2} \end{cases} \tag{25}$$

Mei et al. [53] modified the Filippova and Hanel correlation for the cases where Δ is less than 0.5.

$$\begin{cases} u_{bf} = \dfrac{(\Delta-1)u_f}{\Delta} + \dfrac{u_w}{\Delta} and \chi = (2\Delta - 1)/\tau for \Delta \geq \dfrac{1}{2} \\ u_{bf} = u_f and \chi = (2\Delta - 1)/(\tau - 2) for \Delta < \dfrac{1}{2} \end{cases} \tag{26}$$

Mei et al. [52] investigated curve boundary conditions in LBM and noticed results from previous correlations are less accurate in the nodes with Δ close to one; hence, they modified the last model for Δ higher

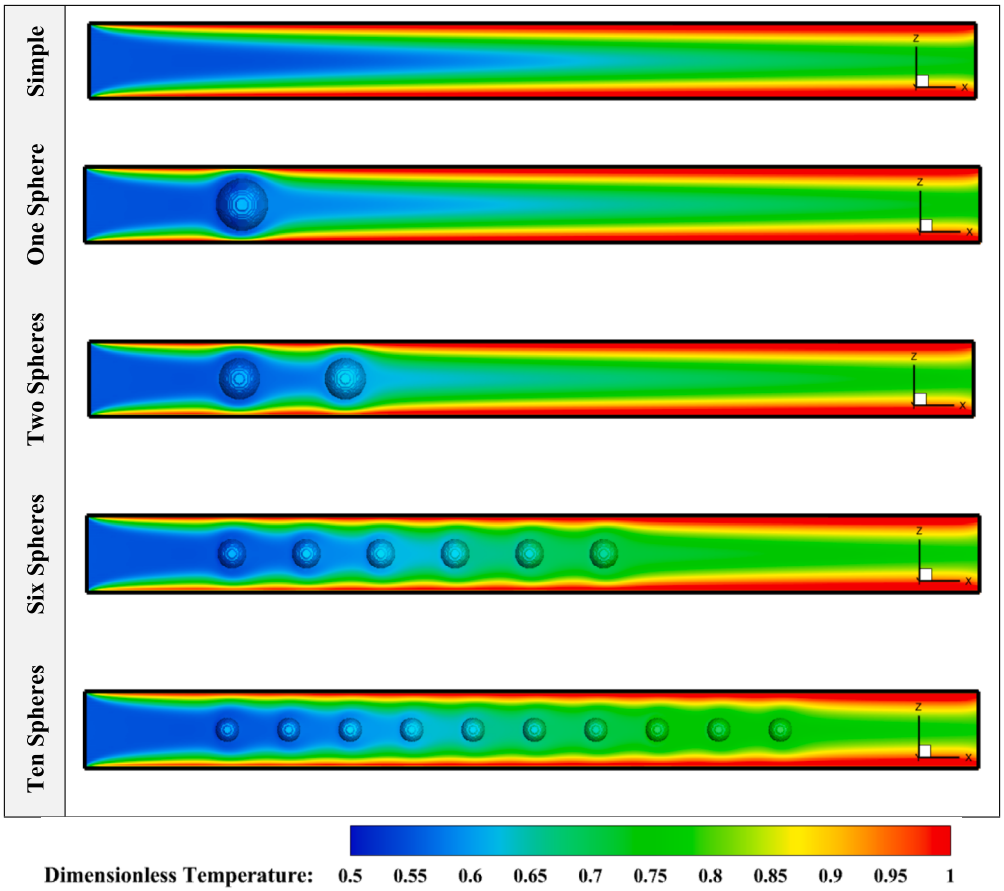

Fig. 8. Non-dimensional temperature intensity contours in a computational domain slice (y/H = 30) for different scenarios.

than ½ to improve the accuracy as below:

$$u_{bf} = \left[1 - \frac{3}{2\Delta}\right]u_f + \frac{3}{2\Delta}u_w and \chi = (2\Delta - 1)/(\tau + 1/2) for \Delta \geq \frac{1}{2} \tag{27}$$

Physical properties of nanofluid in LBM single phase approach

In this study, the correlations derived by Koo and Kleinstreuer [50] are applied to calculate the thermal conductivity model. This model considers Brownian motion in nanofluid's thermal conductivity calculations:

$$k_{eff} = k_{static} + k_{Brownian} \tag{28}$$

$$k_{static} = \frac{k_{pe} + 2k_f + 2(k_{pe} - k_f)(1+\gamma)^3\varphi}{k_{pe} + 2k_f - (k_{pe} - k_f)(1+\gamma)^3\varphi}k_f \tag{29}$$

$$k_{Brownian} = 5 \times 10^4 \beta\varphi\rho_f C_{pf}\sqrt{\frac{KT}{\rho_p d_p}}f(T.\varphi) \tag{30}$$

For K_{pe} in equation (29), Yu and Choi's [51] equivalent nanoparticle thermal conductivity model is applied:

$$k_{pe} = \frac{[2(1-\nu) + (1+\gamma)^3(1+2\nu)]\nu}{-(1-\nu) + (1+\gamma)^3(1+2\nu)}k_p \tag{31}$$

$$\gamma = \frac{t_l}{r_p} \tag{32}$$

$$\nu = \frac{k_l}{k_p} \tag{33}$$

$$k_l = 10k_f \tag{34}$$

For $f(T, \varphi)$ and β factors addressed in the above equations, Vajjha and Das [55] model is applied, which is valid in a wider range of temperatures and nanoparticle size:

$$f(T.\varphi) = \left(2.8217 \times 10^{-2}\varphi + 3.917 \times 10^{-3}\right)\frac{T}{T_0} + \left(-3.0669 \times 10^{-2}\varphi - 3.91123 \times 10^{-3}\right) \tag{35}$$

$$\beta = 8.4407(100\varphi)^{-1.07304} \tag{36}$$

In the experimental investigation conducted by Sharifpur et al. [56], the following equation is utilized to describe the density of the nanofluid:

$$\rho_{nf} = \frac{\varphi\rho_p + (1-\varphi)\rho_f}{(1-\varphi) + \varphi(r_p + t_l)^3/{r_p}^3} \tag{37}$$

$$t_l = -0.0002833r_p^2 + 0.0475r_p - 0.1417 \tag{38}$$

To calculate nanofluids' viscosity, the Brikman model [57] is used. This model considers a solid–liquid interfacial layer; hence, the volume fraction is substituted with an equivalent volume fraction:

$$\frac{\mu_{nf}}{\mu_f} = \frac{1}{(1-\varphi_e)^{2.5}} \tag{39}$$

Below correlations are used for nanofluid's specific heat capacity, thermal diffusivity, and Kinematic viscosity, which have been applied by several authors [58]:

$$\rho_{nf}c_{p.nf} = \varphi\rho_p c_{p.p} + (1-\varphi)\rho_f c_{p.f} \tag{40}$$

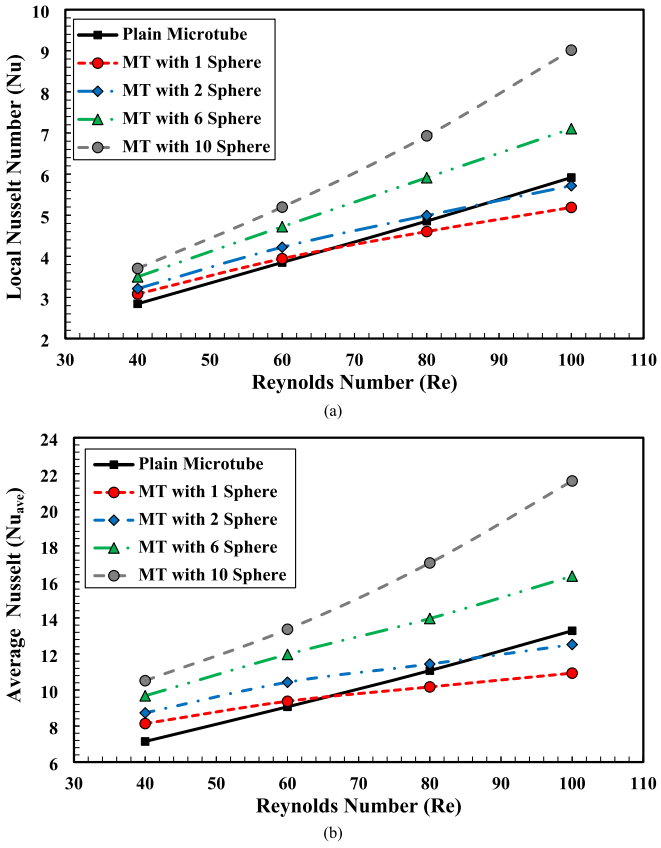

Fig. 9. Influence of sphere number on the local Nusselt number: (a) at 3,000 μm from the entrance of the microtube, (b) at 5,000 μm from the microtube entrance versus various Reynolds numbers.

$$\alpha_{nf} = \frac{k_{eff}}{\rho_{nf} c_{p.nf}} \tag{41}$$

$$\vartheta_{nf} = \frac{\mu_{nf}}{\rho_{nf}} \tag{42}$$

Table 2 presents the thermophysical properties of the base fluid (water), and the nanoparticle.

Convergence criteria

The convergence criteria applied for temperature and velocity in our home-made 3D LBM code are as follows:

$$\frac{\sqrt{\sum_{i,j,k}\left(u_{i,j,k}^{n+1} - u_{i,j,k}^{n}\right)^2}}{\sqrt{\sum_{i,j,k}\left(u_{i,j,k}^{n+1}\right)^2}} = CCF_1 \tag{43}$$

$$\frac{\sqrt{\sum_{i,j,k}\left(T_{i,j,k}^{n+1} - T_{i,j,k}^{n}\right)^2}}{\sqrt{\sum_{i,j,k}\left(T_{i,j,k}^{n+1}\right)^2}} = CCF_2 \tag{44}$$

where the CCF_1 and CCF_2 are equal to 10^{-6}.

Grid Independency and validation analysis

A custom 3D LBM FORTRAN code was developed to analyze how a 2 % Al_2O_3-Water nanofluid behaves in a circular microchannel. To ensure accuracy, four different grid sizes were tested: 40 × 40 × 456, 50 × 50 × 570, 60 × 60 × 684, and 70 × 70 × 798. The outlet temperature was compared across all examined grids. According to Table 3, the 60 × 60 × 684 grid showed the most consistent results, with negligible variation

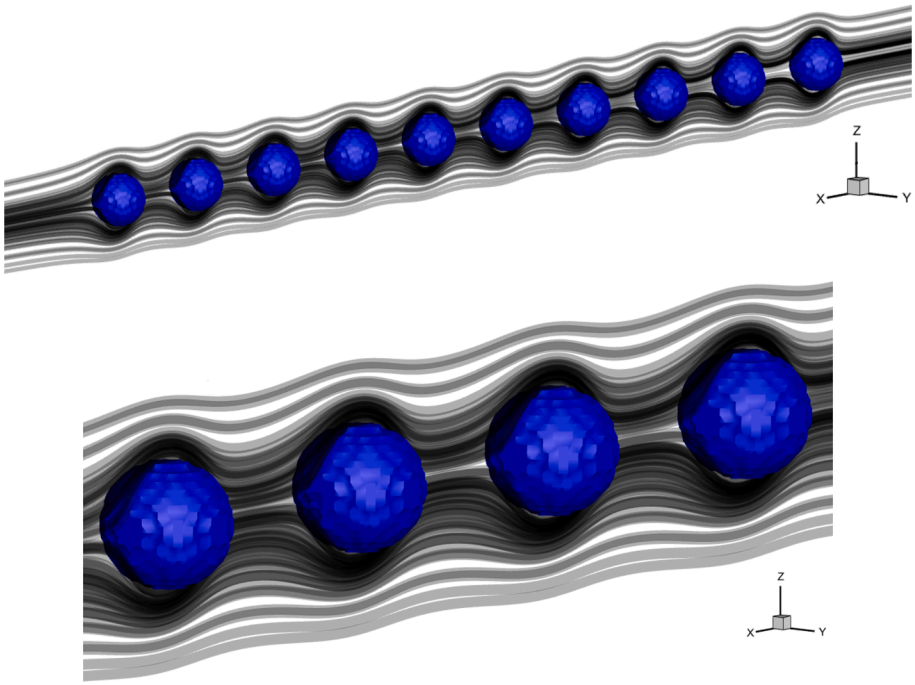

Fig. 10. The fluid flow streamlines passing through the spheres within the channel.

compared to the larger 70 × 70 × 798 grid.

To verify the model, the local Nusselt number for the standard microtube was compared against the results obtained by Salman et al. [16]. Fig. 4a displays this comparison, showing acceptable percentage differences. Also, as the second validation evaluation, the current numerical analysis is validated by comparing the distribution of the local Nusselt number of the plain backward-facing step microchannel (without any sphere) with the experimental results of Kherbeet et al. [59]. The study's findings agree with the experimental data, as shown in Fig. 4b. The graph's percentage differences, which might result from experimental uncertainties and heat dissipations, are presented in tables below each figure.

The analytical results from Kays and Crawford [60], derived for a parallel-plane duct with two surfaces subjected to heat fluxes $\ddot{q}_1$ and $\ddot{q}_2$, respectively, are utilized to validate the proposed thermal LBM model, as the third validation analysis. Heat flux ratios $r_q=\ddot{q}_2/\ddot{q}_1$ of 0.5, 1, and 1.5 are examined. Table 4 presents the average Nusselt numbers of both surfaces, Nu_1 and Nu_2. The comparison shows outstanding agreement between the LBM results and the analytical data from [60], with a maximum relative error of about 1.3 % for both surfaces.

Data processing method

In the calculation of heat flux through the microtube wall, the following formula is utilized [17]:

$$q = \frac{\dot{m} c_{p,nf} (T_{out} - T_{in})}{A_w} \tag{45}$$

where A_w denotes the area of the microtube's wall and $C_{p,nf}$ is the specific heat of the nanofluid. This equation calculates the heat flux transferred through the microtube wall based on the temperature difference between the microtube's outlet (T_{out}) and inlet (T_{in}).To determine the average heat transfer coefficient h_{ave} and average Nusselt number, one can employ the following equations [17]:

$$h_{ave} = \frac{q}{(T_w - T_b)} \tag{46}$$

here, T_w refers to the mean temperature of the microtube surface, and T_b denotes the mean temperature of the bulk fluid. These parameters are essential for evaluating heat transfer efficiency within the microtube. Finally, the average Nusselt number is calculated using the relationship [17]:

$$Nu_{ave} = \frac{h_{ave} D_h}{k} \tag{47}$$

where D_h is the hydraulic diameter of the microtube, and k is the thermal conductivity of the nanofluid. These equations are fundamental for assessing the microtube's thermal performance and the nanofluid's effectiveness in enhancing heat transfer.

Results and discussions

Al_2O_3-Water nanofluid containing particles of 47 nm size at a volume concentration of 2 % was used to study how different arrangements of spherical objects affect their behavior in a microtube. The arrangements included 1, 2, 6, and 10 spheres along the microtube's centerline. The porosity (ε = 83 %) and entrance length of the microtube were kept constant across all arrangements. The distance between the centers of spheres was maintained at five times their radius for each arrangement. A uniform heat flux of 75 kW.m^{-2} was applied to the microtube wall. Numerical simulations covered Reynolds numbers (Re) ranging from 40 to 100, corresponding to inlet velocities of 0.064 m.s^{-1} to 0.16 m.s^{-1}. A 3D home-made LBM code was employed to analyze the heat transfer characteristics of the nanofluid, focusing on parameters such as average Nusselt number, average outlet temperature, average microtube wall temperature, and local Nusselt number for each scenario.

Fig. 5a and 5b, present the microtube wall temperature and microtube outlet temperature variations with the total number of spherical objects. These figures illustrate how the arrangement of spheres influences the hydrothermal performance of the microtube. Fig. 5a depicts the outlet temperatures observed across all scenarios. It highlights a consistent trend: as the Reynolds number increases, the outlet temperature decreases for both the bare microtube and those equipped with 1, 2, 6, or 10 spherical objects. Notably, the microtube containing 10 spheres exhibits the highest outlet temperature at higher Reynolds numbers. In contrast, the microtube with just one sphere consistently shows the lowest outlet temperature across all Reynolds numbers, except at Re = 40, where the plain microtube records the lowest temperature. At Re = 40, the plain microtube records the lowest outlet temperature due to insufficient flow disruption and limited convection, as conduction dominates at this low Reynolds number. The single-sphere configuration slightly enhances mixing but not enough to maintain a significantly higher outlet temperature. As the Reynolds number increases, convection becomes dominant, and even minimal flow disruption from one sphere improves heat transfer, leading to higher outlet temperatures compared to the plain microtube.

According to the data in Fig. 5b, increasing the Reynolds Number decreases the microtube wall temperature across all scenarios. Furthermore, the microtube wall temperature is consistently lower in cases where spherical objects are present compared to the plain microtube. This indicates that incorporating spherical objects improves the heat transfer efficiency of the microtubes. Notably, while the temperature difference between the configurations with 1 and 2 spherical objects is minimal, both setups exhibit lower wall temperatures than the plain microtube.

Fig. 6 displays velocity magnitude contours in a computational domain slice (y/H = 30) for different cases. These contours provide insights into the dynamics of fluid movement and thermal transfer within various configurations. Fig. 6 illustrates how inserting spheres into a microtube creates transverse flows inside, disrupting the boundary layer near the microtube wall. This disruption is most prominent when there is only one sphere, which is noticeable due to the distance between the sphere and the microtube wall.

As more spheres are added, each sphere's impact on the boundary layer decreases, mainly because the spheres are smaller in diameter while maintaining constant porosity. Despite this minimal effect, multiple spheres induce additional transverse flows along the microtube, enhancing thermal exchange between the fluid and the microtube surface.

Fig. 7a and 7b illustrate the influence of spheres on the thermal performance. Reynolds number increases, the average Nusselt number generally rises across all microtube configurations as illustrated in Fig. 7a. Microtubes with 6 and 10 spheres consistently show higher average Nusselt numbers than the plain microtube, indicating improved thermal performance resulting from including spheres within the range studied. However, for microtubes with 1 and 2 spheres, this trend varies with the Reynolds number, showing less steep increases as the Reynolds number increases. At Re = 100, both cases exhibit lower average Nusselt numbers than the plain microtube, possibly due to the sphere size affecting flow dynamics.

In Fig. 7b, the thermal performance varies with the sphere count across Reynolds numbers 40–100. Generally, increasing the number of spheres results in higher heat transfer rates, underscoring the enhanced heat transfer capabilities facilitated by spherical objects in the microtube configurations. Fig. 7b shows the heat transfer rates at different Reynolds numbers across the investigated cases. The trends observed mirror those in Fig. 7a, where higher Reynolds numbers correspond to improved heat transfer rates. Notably, except for configurations with 1 or 2 spheres at higher Reynolds numbers, all other cases demonstrate higher heat transfer rates than the plain microtube. At lower Reynolds numbers, the differences between configurations are minimal, but these

differences become more significant as Reynolds numbers increase. The presence of 1 or 2 spheres does not notably enhance the heat transfer rate, suggesting that fewer larger spheres may not effectively disrupt the flow and improve heat transfer within the microtube.

Fig. 8 illustrates the dimensionless temperature distribution contours in a computational domain slice (y/H = 30) for various configurations. Including spherical inserts disrupts the thermal boundary layer, enhancing thermal stratification near the heated wall. Notably, the configurations with more spheres (e.g., six and ten) exhibit a more uniform temperature distribution than those with fewer spheres or the plain microtube. This indicates that while a single sphere creates localized disruptions, multiple spheres lead to a cumulative effect, enhancing overall heat transfer. These findings highlight the importance of optimizing the number of spheres to achieve efficient thermal performance.

Fig. 9a and 9b show the local Nusselt numbers for all cases at two positions: X = 3,000 μm and X = 5,000 μm from the microtube entrance. The profiles of the local Nusselt number exhibit a pattern comparable to that of the average Nusselt number (Fig. 7a) across all Reynolds numbers. At positions farther from the entrance (X = 3,000 μm and X = 5,000 μm), the local Nusselt numbers exhibit sharper variations, emphasizing more pronounced variations between cases at different Reynolds numbers. The maximum local Nusselt number is recorded in the configuration with 10 spheres in both figures. The variations between models become more prominent at higher Reynolds numbers than at lower Reynolds numbers.These results emphasize how spherical inserts affect local heat transfer within the microtube, especially in configurations with multiple spheres and greater distances from the entrance.

At Reynolds numbers Re = 40 and Re = 60, all configurations with spherical inserts show higher local Nusselt numbers than the plain microtube. After Re = 60, a change in the pattern of the local Nusselt number profiles is observed. This alteration is evident in every configuration, excluding the single-sphere configuration, which shows the minimum local Nusselt number at Re = 80. Moreover, at Re = 100, The configurations with 1 and 2 spherical objects display lower Nusselt numbers than the standard microtube, with the single-sphere model having the smallest Nusselt number.

Fig. 10 illustrates the 3D flow patterns at Re = 40 within the microtube, highlighting the distinct crossflow patterns generated behind the spheres. These patterns indicate flow disruption caused by the spheres, a mechanism that enhances heat transfer rates.

Conclusion

The study investigated the laminar forced convection of a 4 % Al_2O_3-water nanofluid in a microtube modified with spherical inserts, treating it as a microporous medium. Using 3D lattice Boltzmann method simulations, several key findings were identified:

- Outlet temperatures decreased with increasing Reynolds numbers across all cases, including plain microtubes and microtubes with varying numbers of spherical inserts (1, 2, 6, and 10).
- The microtube with 10 spheres consistently showed the highest outlet temperatures, while the microtube with one sphere generally exhibited the lowest, except at Re = 40, where the plain microtube had the lowest.
- Wall temperatures in microtubes with spherical inserts were consistently lower than in plain microtubes, indicating enhanced heat transfer performance. The difference in wall temperatures between configurations with 1 and 2 spheres was minimal, but both were lower than plain microtubes.
- At Re = 100, the average Nusselt numbers for microtubes with 6 and 10 spheres were around 22.95 % and 31.01 % greater than that of the plain microtube, respectively.
- Configurations with fewer spheres, implying larger sphere sizes, exhibited less noticeable effects from spherical inserts.

The study explored strategies involving microporous structures and nanofluids to improve heat transfer rates in microtubes. It focused on the influence of sphere diameter, number, and Reynolds number on nanofluid hydrothermal behavior within the microtube. Future research could further investigate the impact of fixed nanofluid properties, such as type, volume concentration, and nanoparticle diameter, to deepen understanding of their role in microtube heat transfer enhancement.

CRediT authorship contribution statement

Saboura Yousefi: Writing – original draft, Validation, Software, Investigation, Formal analysis, Conceptualization. **Mostafa Mahdavi:** Writing – review & editing, Supervision, Software, Resources, Project administration. **Seyed Soheil Mousavi Ajarostaghi:** Writing – review & editing, Validation, Methodology, Investigation. **Mohsen Sharifpur:** Writing – review & editing, Supervision, Resources, Project administration. **Magda Abd El-Rahman:** Review & editing, Funding acquisition.

Declaration of competing interest

The authors declare that they have no known competing financial interests or personal relationships that could have appeared to influence the work reported in this paper.

Acknowledgment

Magda Abd El-Rahman extends their appreciation to the Deanship of Research and Graduate Studies at King Khalid University for funding this work through Large Research Project under grant number RGP2 /39 /46.

Data availability

No data was used for the research described in the article.

References

[1] Ma H, He B, Su L, He D. Heat transfer enhancement of nanofluid flow at the entry region of microtubes. Int J Therm Sci 2023;184:107944.
[2] Choi S. Enhancing thermal conductivity of fluids with nanoparticles. Dev Appl Non-Newtonian Flows 1995:99–105.
[3] Meyer J, Nwosu P, Sharifpur M, Ntumba T. Parametric analysis of effective viscosity models for nanofluids. Proceedings of the the ASME 2012 Int. Mech. Eng. Congr. Expo., Houston. 2012.
[4] Jang SP, Choi SU. Cooling performance of a microchannel heat sink with nanofluids. Appl Therm Eng 2006;26:2457–63.
[5] Adnan KU, Rahman Z, Mahmood SU, Khan A, Ali Z Li, Tlili I. Enhanced thermal study in hybrid nanofluid flow in a channel motivated by graphene/Fe3O4 and Newtonian heating. Results Eng 2024;21:101772.
[6] Kherbeet A, Mohammed H, Munisamy K, Salman B. The effect of step height of microscale backward-facing step on mixed convection nanofluid flow and heat transfer. Int J Heat Mass Transf 2014;68:554–66.
[7] Salman S, Abu Talib A, Saadon S, Hameed Sultan M. Hybrid nanofluid flow and heat transfer over backward and forward steps: A review. Powder Technol 2020; 363:448–72.
[8] Yang D, Sun B, Xu T, Liu B, Li H. Experimental and numerical study on the flow and heat transfer characteristic of nanofluid in the recirculation zone of backward-facing step microchannels. Appl Therm Eng 2021;199:117527–8137.
[9] Masoud Ali A, Angelino M, Rona A. Physically consistent implementation of the mixture model for modelling nanofluid conjugate heat transfer in minichannel heat sinks. Appl Sci 2022;12:7011.
[10] Sharifpur M, Ntumba T, Meyer JP. Parametric analysis of effective thermal conductivity models for nanofluids. In: ASME Int. Mech. Eng. Congr. Expo. American Society of Mechanical Engineers; 2012. p. 1–11.
[11] Yousefi S, Mahdavi M, Mousavi Ajarostaghi SS, Sharifpur M. Hydrothermal behavior of nanofluid flow in a microscale backward-facing step equipped with dimples and ribs; Lattice Boltzmann method approach. Therm Sci Eng Prog 2023; 43:101987.

[12] Ali A, Barman A, Das S. EDL aspect in cilia-regulated bloodstream infused with hybridized nanoparticles via a microtube under a strong field of magnetic attraction. Therm Sci Eng Prog 2022;36:101510.
[13] Shimizu S, Nishizaki K, Konish S. Openable double-microtube structure driven by pneumatic balloon actuator arrays for tubular organ-on-a-chip. IEEJ Trans Electr Electron Eng 2024;19(5):872–5.
[14] Mitchell MJ, Chen CS, Ponmudi V, Hughes AD, King MR. E-selectin liposomal and nanotube-targeted delivery of doxorubicin to circulating tumor cells. J Control Release 2012;160:609–17.
[15] Rahmati AR, Ali Akbari O, Marzban A, Toghraie D, Karimi R, Pourfattah F. Simultaneous investigations the effects of non-Newtonian nanofluid flow in different volume fractions of solid nanoparticles with slip and no-slip boundary conditions. Therm Sci Eng Prog 2018;5:263–77.
[16] Salman B, Mohammed H, Kherbeet AS. Heat transfer enhancement of nanofluids flow in microtube with constant heat flux. Int Commun Heat Mass Transf 2012;39:1195–204.
[17] Salman B, Mohammed H, Kherbeet A. Numerical and experimental investigation of heat transfer enhancement in a microtube using nanofluids. Int Commun Heat Mass Transf 2014;59:88–100.
[18] Salman BH, Mohammed HA, Munisamy KM, Kherbeet AS. Three-dimensional numerical investigation of nanofluids flow in microtube with different values of heat flux. Heat Transf Asian Res 2015;44(7):599–619.
[19] Karimzadehkhouei M, Khalili Sadagh A, Motezakker AR, Akgönül S, Ozbey A, Sendur K, et al. Experimental and numerical investigation of inlet temperature effect on convective heat transfer of γ-Al2O3/water nanofluid flows in microtubes. Heat Transf Eng 2019;40:738–52.
[20] Lappa M, Inam S. Large eddy simulation of three-dimensional hybrid forced-buoyancy convection in channels with a step. Int J Heat Mass Transf 2023;202:123767.
[21] Shan X, Chen H. Lattice Boltzmann model for simulating flows with multiple phases and components. Phys Rev e 1993;47:1815–9.
[22] Kefayati G, Hosseinizadeh S, Gorji M, Sajjadi H. Lattice Boltzmann simulation of natural convection in tall enclosures using water/SiO2 nanofluid. Int Commun Heat Mass Transf 2011;38:798–805.
[23] Zhou L, Xuan Y, Li Q. Multiscale simulation of flow and heat transfer of nanofluid with lattice Boltzmann method. Int J Multiphase Flow 2010;36:364–74.
[24] Xuan Y, Yao Z. Lattice Boltzmann model for nanofluids. Heat Mass Transf 2005;41:199–205.
[25] Ren J, Liu X, Gao Y. Axisymmetric lattice Boltzmann model with slip boundary conditions for liquid flows in microtube. Eur J Mech B Fluids 2021;89:430–44.
[26] Mustafa J, Alqaed S, Husain S, Sharifpur M. Impact of five obstacles with constant temperatures on the mixed convection flow of water/copper nanofluid in a rectangular cavity with a magnetic field. Results Phys 2024;57:107424.
[27] Huang H, Lee T, Shu C. Lattice Boltzmann method simulation gas slip flow in long microtubes. Int J Numer Methods Heat Fluid Flow 2007;17(6):587–607.
[28] Yang Y, Lai F. Lattice Boltzmann simulation of heat transfer and fluid flow in a microchannel with nanofluids. Heat Mass Transf 2011;47:1229–40.
[29] Xu A, Zhao T, Shi L, Yan X. Three-dimensional lattice Boltzmann simulation of suspensions containing both micro- and nanoparticles. Int J Heat Fluid Flow 2016;62:560–7.
[30] Abdollahzadeh Y, Mehrpooya M, Mousavian SMA, Moqtaderi H. Modeling and simulation of nanofluid in low Reynolds numbers using two-phase Lattice Boltzmann method based on mixture model. Chem Eng Res Des 2023;192:402–11.
[31] Zhang N, Liu D. LBM modeling of three-dimensional mixed convection in CZ crystal growth on curvilinear coordinates system. Results Phys 2024;61:107754.
[32] Sorour Amini H, Mohammadi A. Microparticle separation using dielectrophoresis-assisted inertial microfluidics: A GPU-accelerated immersed boundary–lattice Boltzmann simulation. Phys Rev E 2023;107:035307.
[33] Nee A, Chamkha AJ. A simplified GPU implementation of the hybrid lattice boltzmann model for three-dimensional high rayleigh number flows. Int J Appl Mech 2023;15(06):2350047.
[34] Akter UH, Hasan MF, Molla MM. A parallel computational study of power-law non-Newtonian nanofluid in a C-shaped enclosure by multiple-relaxation-time lattice Boltzmann simulation. Int J Model Simul 2024:1–30.
[35] Buonomo B, Manca O, Lauriat G. Forced convection in micro-channels filled with porous media in local thermal non-equilibrium conditions. Int J Therm Sci 2014;77:206–22.
[36] Nield DA, Kuznetsov AV. Forced convection with slip-flow in a channel or duct occupied by a hyper-porous medium saturated by a rarefied gas. Transp Porous Media 2006;64:161–70.
[37] Kuznetsov AV, Nield DA. Thermally developing forced convection in a porous medium occupied by a rarefied gas: parallel plate channel or circular tube with walls at constant heat flux. Transp Porous Media 2009;76:345–62.
[38] Haddad OM, Al-Nimr MA, Sari MS. Forced convection gaseous slip flow in circular porous micro-channels. Transp Porous Media 2007;70:167–79.
[39] Hooman K. Slip flow forced convection in a microporous duct of rectangular cross-section. Appl Therm Eng 2009;29(5–6):1012–9.
[40] Li S, Dimitrienko Y. Least squares finite element simulation of local transfer for a generalized Newtonian fluid in 2D periodic porous media. J Non-Newtonian Fluid Mech 2023;316:105032.
[41] Plant RD, Hodgson GK, Impellizzeri S, Saghir MZ. Experimental and numerical investigation of heat enhancement using a hybrid nanofluid of copper oxide/alumina nanoparticles in water. J Therm Anal Calorim 2020;141:1951–68.
[42] Wang K, Tavakkoli F, Wang S, Vafai K. Forced convection gaseous slip flow in a porous circular microtube: An exact solution. Int J Therm Sci 2015;97:152–62.
[43] Nojoomizadeh M, Karimipour A, Firouzi M, Afrand M. Investigation of permeability and porosity effects on the slip velocity and convection heat transfer rate of Fe3O4/water nanofluid flow in a microchannel while its lower half filled by a porous medium. Int J Heat Mass Transf 2018;119:891–906.
[44] Papazian K, Al Hajaj Z, Saghir MZ. Thermal performance of a heated pipe in the presence of a metal foam and twisted tape inserts. Fluids 2020;5(4):195.
[45] Ibrahim M, Saeed T, Riahi Bani F, Naghdi Sedeh S, Chu Y-M, Toghraie D. Two-phase analysis of heat transfer and entropy generation of water-based magnetite nanofluid flow in a circular microtube with twisted porous blocks under a uniform magnetic field. Powder Technol 2021;384:522–41.
[46] Derikvand M, Rahmati AR. Numerical investigation of power-law hybrid nanofluid in a wavy micro-tube with the hydrophobic wall and porous disks under a magnetic field. Int Commun Heat Mass Transf 2021;129:105633.
[47] Zhu Q, Xuan Y. Pore scale numerical simulation of heat transfer and flow in porous volumetric solar receivers. Appl Therm Eng 2017;120:150–9.
[48] Habib R, Karimi N, Yadollahi B, Doranehgard MH, Li LKB. International Journal of Heat and Mass Transfer 153 (2020) 119657_A pore-scale assessment of the dynamic response of forced convection in porous media to inlet flow modulations. Int J Heat Mass Transf 2020;153:119657.
[49] Cheng L-C, Wong S-C. Pore-scale numerical simulation and LTNE analysis for fully-developed forced convective heat transfer in packed beds of mono-sized rough spheres covering near-wall and core regions. Int J Heat Mass Transf 2023;208:124047.
[50] Wang M, Bu S, Zhou B, Gong B, Li Z, Chen D. Pore-scale simulation on flow and heat transfer characteristics in packed beds with internal heat sources at low Reynolds numbers. Int J Heat Mass Transf 2023;213:124325.
[51] Mohamad AA. Lattice Boltzmann Method. Calgary: Springer; 2011.
[52] Mei R, Shyy W, Yu D, Luo L-S. Lattice boltzmann method for 3-D flows with curved boundary. J Comput Phys 2000;161:680–99.
[53] Mei R, Luo L-S, Shyy W. An accurate curved boundary treatment in the lattice Boltzmann method. J Comput Phys 1999;155:307–30.
[54] Filippova O, Hanel D. Grid refinement for lattice-BGK models. J Comput Phys 1998;147:219–28.
[55] Vajjha R, Das D. Specific heat measurement of three nanofluids and development of new correlations. J Heat Transf 2009;131(7):1–7.
[56] Sharifpur M, Yousefi S, Meyer JP. A new model for density of nanofluids including nanolayer. Int Commun Heat Mass Transf 2016;78:168–74.
[57] Brikman H. The viscosity of concentrated suspensions and solution. J Chem Phys 1952;20(4):571–81.
[58] Yu W, Choi S. The role of interfacial layers in the enhanced thermal conductivity of nanofluids A renovated Maxwell mode. J Nanopart Res 2003;5:167–71.
[59] Kherbeet AS, Mohammed HA, Salman BH, Ahmed HE, Alawi OA. Experimental and numerical study of nanofluid flow and heat transfer over microscale backward-facing step. Int J Heat Mass Transf 2014;79:858–67.
[60] Kays WM, Crawford M. Solutions Manual. In: Convective Heat and Mass Transfer. 3rd ed. New-York, Problem: McGraw-Hill; 1993. p. 9.